Control Engineering Practice 144 (2024) 105836

Contents lists available at ScienceDirect

Control Engineering Practice

journal homepage: www.elsevier.com/locate/conengprac

Sliding-mode control of a soft robot based on data-driven sparse identification

Dimitrios Papageorgiou [a,*], Guðrún Þóra Sigurðardóttir [a], Egidio Falotico [b], Silvia Tolu [a]

[a] DTU Electrical and Photonics Engineering, Elektrovej 326, Kgs. Lyngby, 2800, Denmark
[b] BioRobotics Instituteand the Department of Excellence in Robotics and AI, Scuola Superiore Sant'Anna, Pontedera Pisa, 56025, Italy

ARTICLE INFO

Keywords:
Soft robots
Data-driven model
Sparse regression
Nonlinear system identification
Sliding mode control
Adaptive estimation

ABSTRACT

Soft robots are increasingly finding their way into many applications, especially those involving manipulation of sensitive and delicate objects or interaction with humans. However, their high-compliance characteristics pose considerable challenges in obtaining low-complexity yet accurate dynamical models that are suitable for advanced feedback control. This paper proposes a framework for end-effector positioning of a soft robot. First, physics-informed sparse regression is used for deriving a nonlinear mathematical model of the robot dynamics. Then, a control scheme comprising a super-twisting sliding mode controller and a nonlinear input estimator is designed for the positioning of the robot end-effector. Conditions for uniform asymptotic stability of the closed-loop system are given. Finally, experimental tests carried on a real soft robot show the efficacy of the proposed design and its tracking accuracy.

1. Introduction

Soft robots made of lightweight and flexible materials are becoming increasingly popular in a multitude of applications such as medical operations and patient rehabilitation routines (Cianchetti, Laschi, Menciassi, & Dario, 2018). Their compliant morphology allows them to manipulate fragile objects and, by extension, facilitates safe human–robot interaction (Lipson, 2014; Rus & Tolley, 2015).

The development of dynamic controllers for soft robots is important if the latter are to achieve the level of accuracy and agility in movements of the biological systems that inspired their design. A survey on the different soft robot control approaches was presented in Thuruthel, Ansari, Falotico, and Laschi (2018). Although model-free (Thuruthel, Falotico, Renda, & Laschi, 2017), open-loop (Reinhart, Shareef, & Steil, 2017) and learning-based control strategies (Jiang et al., 2017; Wang, Li, & Kwok, 2021) are able to achieve good performance for specific tasks, they are difficult to generalise and do not provide theoretical guarantees on the stability of the system. On the other hand, leveraging powerful control schemes from the arsenal of model-based control theory (Della Santina, Duriez, & Rus, 2021; Mazare, Tolu, & Taghizadeh, 2022) requires accurate and explicit mathematical models.

Unlike rigid-link industrial robotic manipulators that are efficiently described by first-principle models, soft robots and in particular *continuum robots* are characterised by heavy nonlinearities in their dynamics, which are hard to accurately model. Their theoretically infinite dimensionality poses a significant challenge in applying analytical methods such as Euler–Lagrange formalism (Falkenhahn, Mahl, Hildebrandt, Neumann, & Sawodny, 2014) and often results in reduced accuracy or computationally heavy control algorithms. Static and kinematic models and low-order dynamic approximations (Thuruthel, Renda, & Iida, 2020) promote simpler and computationally efficient control designs. However, they introduce several steady-state assumptions such as the *constant curvature* approximation, which ignores any effects of gravitational forces and payload weights that affect the shape of the robot. These assumptions can be very limiting in terms of performance since the resulting control schemes are either restricted to a limited part of the robot task space or have reduced accuracy and robustness. On the other hand, detailed neural-network models such as those presented in Melingui, Merzouki, Mbede, Escande, and Benoudjit (2014), Thuruthel et al. (2017), Parvaresh and Moosavian (2021) and Kim et al. (2021) may yield accurate descriptions of the robot dynamics but – similar to the learning-based control methods – at the cost of high-dimensionality or lack of generalisability. This severely hinders the application of powerful model-based control methods that in general do not scale well with dimensionality. Koopman operator theory was proposed in Bruder, Remy, and Vasudevan (2019) for obtaining a dynamical model of a soft robot. The main contribution

* Corresponding author.
E-mail addresses: dimpa@dtu.dk (D. Papageorgiou), gudrunthoras@gmail.com (G. Sigurðardóttir), egidio.falotico@santannapisa.it (E. Falotico), stolu@dtu.dk (S. Tolu).

https://doi.org/10.1016/j.conengprac.2023.105836
Received 30 May 2023; Received in revised form 21 November 2023; Accepted 21 December 2023
Available online 30 December 2023

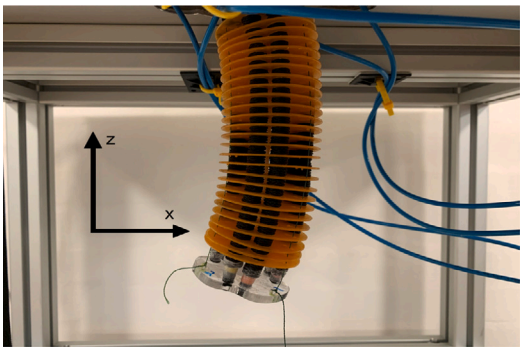

Fig. 1. The soft robot system.

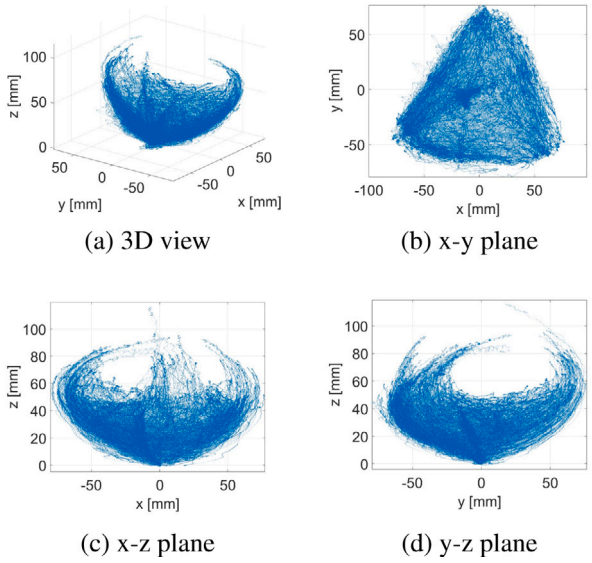

Fig. 2. Perspective (a), top (b) and side (c,d) views of the entire workspace $\mathscr{W}$ of the robot. Each blue dot corresponds to a position measurement of the robot while data was sampled for SINDYc. (For interpretation of the references to colour in this figure legend, the reader is referred to the web version of this article.)

was the explicit description of the robot dynamics as a linear combination of monomial basis functions. Sparse Identification of Nonlinear Dynamics (SINDy) (Brunton, Proctor, & Kutz, 2016a) and SINDy with Control (SINDYc) (Brunton, Proctor, & Kutz, 2016b) have provided an alternative solution to Koopman operators. The authors proposed a framework for identifying nonlinear dynamics that are *parsimonious* and that embed physics principles into the derived models. This is done by utilising a large library of basis functions that relate to the physics of the system to be modelled. After an iterative process, the functions that are not significant are rejected yielding sparse models of low dimensionality. The embedding of physical laws in SINDy models was further explored in Machado and Jones (2023), where the authors developed an extension, namely the SINDy with Side Information (SINDy-SI) based on Sum-of-Squares programming.

SINDYc was used in Li, Wang, and Zhu (2022) for obtaining scalar Single-Input Single-Output (SISO) models of viscoelastic dielectric elastomer actuators, which are widely used in soft robotic applications. The 3rd-order dynamics of the conduit displacements of a robotic esophagus were discovered in Bhattacharya, Cheng, and Xu (2019) by using SINDYc. The sparsity and accuracy of SINDYc models allows for the utilisation of advanced model-based control methods such as Model Predictive Control (MPC) and nonlinear control, which not only ensure high accuracy but also provide the framework to theoretically assess stability of the closed-loop system. An integrated scheme of SINDYc and MPC was introduced in Kaiser, Kutz, and Brunton (2018). The method was applied in Bhattacharya, Hashem, Cheng, and Xu (2021) for control of the robotic esophagus system. A combination of Koopman operators with SINDy-MPC was proposed in Wang et al. (2022) for controlling soft actuators.

The parsimony of SINDYc models allows for adaptation to rapid system changes by means of rediscovering the new dynamics (Quade, Abel, Nathan Kutz, & Brunton, 2018). This feature is very useful when the applied controller heavily relies on the accuracy of the model such as is the case of MPC (Kaiser et al., 2018). Reiterating the identification of the changed dynamics may, however, be avoided when using robust control strategies. Indeed, variable structure controllers (Emelyanov, 1967) and specifically Sliding Mode Control (SMC) schemes feature strong stability and robustness properties (Utkin, 1992). The STSMC in particular, has been shown (Levant, 1993) to facilitate high accuracy performance with low chattering, which is one of the main challenges in SMC design (Boiko, Fridman, Pisano, & Usai, 2007). Moreover, the low complexity of the STSMC law makes it significantly computationally cheaper than MPC approaches.

This study pursues the development of a nonlinear control scheme for soft robots based on sparse regression modelling. The main contribution of the present work is the synthesis of a SINDYc-STSMC framework for end-effector positioning of a soft robot, which, to the best of the author's knowledge, has not been proposed before. More specifically, SINDYc is employed to derive a low-order dynamical physics-informed model of the soft robot, which is valid in a large subset of the robot workspace and does not adopt any limiting assumptions. The obtained Multiple-Input Multiple-Output (MIMO) dynamics are by definition observable since SINDYc identifies the dynamical behaviour of the measured signals, i.e. all the states are measured. The second part of the proposed framework pertains to the design of a modular cascaded control architecture based on the obtained model that features a STSMC and an online estimator for dealing with the control input nonlinearities. One of the advantages of STSMC is the fact that the inherent robustness of the controller against bounded-rate perturbation allows for *independent control*, i.e. each state can be controlled individually with cross-couplings being treated as perturbations. The input estimator facilitates nonlinear control design as if the input mapping channel were linear. Moreover, there is no limitation in the type of the individual components of the control scheme provided that they satisfy the stability and boundedness criteria of the cascade. These properties are rigorously proven for the selected design of this study. Finally, the applicability and efficacy of the proposed solution is experimentally verified on a real continuum robot platform.

The remainder of the paper is organised as follows: Section 2 describes the soft robot system studied in this paper and details the derivation of its dynamical model. The design of the nonlinear feedback controller and the stability analysis of the closed-loop system is presented in Section 3. Experimental verification of the proposed solution and performance evaluation of the control scheme is given in Section 4. Finally, conclusions are drawn in Section 5 along with some remarks on future work.

2. System description and modelling

2.1. System description

The system used in this study is a soft robot arm that has a continuum structure. Continuum robots differ from rigid-link robots in the way that they can bend and often expand or contract at any point along their structure (Walker, 2013). The soft robot arm can be seen in Fig. 1. It consists of one 205 mm long module that can be bent in different directions when actuated and also slightly contract and expand. The robot has cables and McKibben-based actuators operating at 40 Hz. Let $X_{min}, X_{max}, Y_{min}, Y_{max}, Z_{min}, Z_{max}$ be the extreme values that the robot

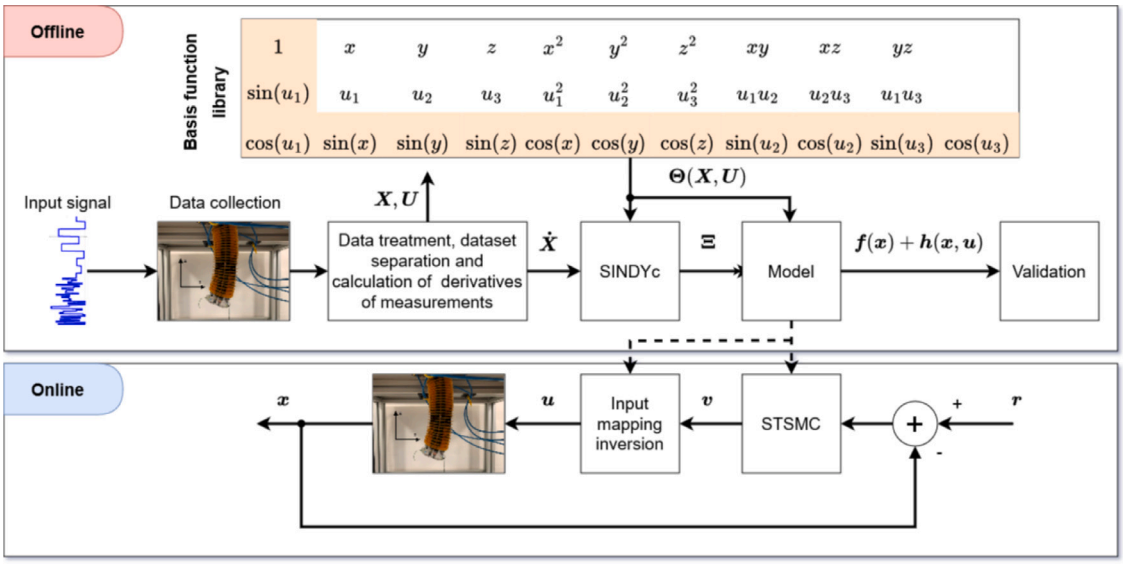

Fig. 3. Schematic diagram of the proposed method. The coloured basis functions were discarded during the sparsification of the algorithm.

end-effector can assume in each coordinate. Then the workspace of the robot shown in Fig. 2 is defined as

$$\mathscr{W} \subset [X_{min}, X_{max}] \times [Y_{min}, Y_{max}] \times [Z_{min}, Z_{max}] \ .$$

Similarly, the set of all allowable control inputs $\boldsymbol{u}$ will be denoted by

$$\mathscr{U} \subset [u_1^{min}, u_1^{max}] \times [u_2^{min}, u_2^{max}] \times [u_3^{min}, u_3^{max}] \ .$$

2.2. Mathematical model

SINDYc is employed in this study to obtain a physics-informed data-driven dynamical model of the soft robot. The motivation for using SINDYc relates to obtaining a *low-dimension* mathematical model that captures the essential dynamical behaviour of the system by incorporating first-principle terms in the basis function library $\boldsymbol{\Theta}(\boldsymbol{x}^T, \boldsymbol{u}^T)$. These terms do not compile the exact first-principle equations, which is very challenging in soft robots, but rather fundamental elements of the kinematics and dynamics (e.g. rotation terms etc.). The objective is to find a library $\boldsymbol{\Theta}(\boldsymbol{x}^T, \boldsymbol{u}^T)$ of nonlinear functions of the system states and inputs and a sparse matrix $\boldsymbol{\Xi}$ of coefficients such that the soft robot dynamics is written as $\dot{\boldsymbol{x}} = \boldsymbol{\Xi}^T \boldsymbol{\Theta}^T(\boldsymbol{x}^T, \boldsymbol{u}^T)$, where $\boldsymbol{u} = \begin{bmatrix} u_1 & u_2 & u_3 \end{bmatrix}^T$ is the inputs vector and $\boldsymbol{x} = \begin{bmatrix} x & y & z \end{bmatrix}^T$ is the state vector consisting of the measured end-effector position in base coordinates.

Fig. 3 shows an overview of the entire proposed scheme with the control strategy integrated as well. Measurement data collected at times t_k, $k = 1, \dots, m$ are arranged into matrices as shown in (1), (2) and (3).

$$\boldsymbol{X} = \begin{bmatrix} x(t_1) & y(t_1) & z(t_1) \\ \vdots & \vdots & \vdots \\ x(t_m) & y(t_m) & z(t_m) \end{bmatrix}, \tag{1}$$

$$\dot{\boldsymbol{X}} = \begin{bmatrix} \dot{x}(t_1) & \dot{y}(t_1) & \dot{z}(t_1) \\ \vdots & \vdots & \vdots \\ \dot{x}(t_m) & \dot{y}(t_m) & \dot{z}(t_m) \end{bmatrix}, \tag{2}$$

$$\boldsymbol{U} = \begin{bmatrix} u_1(t_1) & u_2(t_1) & u_3(t_1) \\ \vdots & \vdots & \vdots \\ u_1(t_m) & u_2(t_m) & u_3(t_m) \end{bmatrix} \tag{3}$$

A sparse regression problem is set up as $\dot{\boldsymbol{X}} = \boldsymbol{\Theta}(\boldsymbol{X}, \boldsymbol{U})\boldsymbol{\Xi}$ where $\boldsymbol{\Theta}(\boldsymbol{X}, \boldsymbol{U})$ is a data matrix. A separate Lasso optimisation (Tibshirani, 1996) is made for each column of $\dot{\boldsymbol{X}}$

$$\arg\min_{\boldsymbol{\xi}_j} \left(\|\dot{\boldsymbol{x}}_j - \boldsymbol{\Theta}(\boldsymbol{X}, \boldsymbol{U})\boldsymbol{\xi}_j\|_2^2 + \lambda \|\boldsymbol{\xi}_j\|_1 \right), \ j = 1, \dots, n$$

to obtain the columns $\boldsymbol{\xi}_j$ of $\boldsymbol{\Xi}$. The usage of ℓ_1 norm in Lasso promotes sparsity and prevents overfitting.

The measurement data gathered from the system consisted of a time vector $\boldsymbol{t} = \begin{bmatrix} t_1 & \cdots & t_m \end{bmatrix}^T$, the inputs to the servos $\boldsymbol{u}$ and the measurements of the robot's end-effector position $\boldsymbol{x}$ at each time. The derivatives $\dot{\boldsymbol{X}}$ were obtained using finite difference approximation. An 80% of the total 652 000 collected data samples was organised in a matrix structure like the one described in Eqs. (1)–(3).

The selection of the nonlinear function library $\boldsymbol{\Theta}(\boldsymbol{x}^T, \boldsymbol{u}^T)$ was based on the implicit knowledge about the system dynamics after considering the elasticity of the cable actuators of the robot. The high coupling between the system inputs and states can be described by polynomial expressions, while the curved shape of the robot motivated the inclusion of trigonometric terms. Therefore $\boldsymbol{\Theta}(\boldsymbol{x}^T, \boldsymbol{u}^T)$ comprised polynomial terms of the type $x^{n_x} y^{n_y} z^{n_z} u_1^{n_1} u_2^{n_2} u_3^{n_3}$ with $n_x + n_y + n_z + \sum_{i=1}^{3} n_i \leq 2$ (e.g. 1, xy, zu_1, u_2^2) as well as trigonometric functions of the states and inputs, i.e. $\sin(x)$, $\sin(y)$, $\sin(z)$, $\cos(x)$, $\cos(y)$, $\cos(z)$, $\sin(u_i)$ and $\cos(u_i)$, $i \in \{1, 2, 3\}$. The identified continuous time model can be written as

$$\dot{\boldsymbol{x}} = \underbrace{\boldsymbol{A}\boldsymbol{x} + \boldsymbol{f}_{\boldsymbol{A}}(\boldsymbol{x})}_{f(x)} + \underbrace{\left[\boldsymbol{B}_1 + \boldsymbol{B}_2(\boldsymbol{x})\right]\boldsymbol{u} + \boldsymbol{g}(\boldsymbol{u})}_{h(x,u)}, \tag{4}$$

with $\boldsymbol{A}$, $\boldsymbol{f}_{\boldsymbol{A}}$, $\boldsymbol{B}_1$, $\boldsymbol{B}_2$ and $\boldsymbol{g}$ given in Table 1. The trigonometric terms were not influential enough to the model response and were eventually discarded during the sparsification.

Validation of the identified nonlinear model was done by using the remaining 20% of the collected data (130 400 samples). The results are shown in Fig. 4. The goodness of the model relates to the performance specifications of each application and can be quantified by several metrics, e.g. the ratio between output RMSE ϵ_j, $j \in \{x,y,z\}$ and accuracy bounds or the coordinates extremes. Since the paper does not focus on a specific application of the soft robot, the evaluation of the model is restricted to the calculation of the *relative* RMSE γ and the associated *model fit* defined by

$$\gamma \triangleq \max\left(\frac{\epsilon_x}{\max|x(t)|}, \frac{\epsilon_y}{\max|y(t)|}, \frac{\epsilon_z}{\max|z(t)|} \right)$$

and fit $= (1 - \gamma) \cdot 100\%$, respectively. Their values were calculated as $\gamma = 0.163$ and fit$= 83.7\%$.

Remark 1. For the identification of the soft robot dynamics, the system was subjected to rich excitation with inputs covering the entire range of the actuator values and at different frequencies as shown in Fig. 5.

Table 1
Dynamical model of soft robot.

$$\boldsymbol{A} = \begin{bmatrix} 0 & 0 & 0 \\ 0 & -1.4044 & 0.7363 \\ 0 & 0 & -6.1535 \end{bmatrix}, \quad \boldsymbol{f_A}(\boldsymbol{x}) \triangleq \begin{bmatrix} 0.17x^2 - 1.22y^2 - 0.145z^2 + 4.92xy + 20.3xz + 0.748yz \\ 3.39x^2 - 1.94y^2 + 3.48z^2 - 1.68xy + 5.63xz + 17.0yz \\ 0.456x^2 + 0.672y^2 + 19.4z^2 - 1.92xy + 1.3xz - 0.0985yz \end{bmatrix}$$

$$\boldsymbol{B_1} = \begin{bmatrix} -1.6909 & 2.0717 & -0.5338 \\ 1.4754 & 1.1778 & -2.9646 \\ 0.3089 & 0.5663 & 0.0359 \end{bmatrix}, \quad \boldsymbol{g}(\boldsymbol{u}) \triangleq \begin{bmatrix} 14.1{u_1}^2 - 8.48{u_2}^2 + 5.9{u_3}^2 - 5.02u_1u_2 - 6.56u_1u_3 + 3.04u_2u_3 \\ -11.3{u_1}^2 - 4.67{u_2}^2 + 19.5{u_3}^2 + 1.54u_1u_2 + 3.15u_1u_3 - 1.25u_2u_3 \\ 1.05{u_1}^2 + 2.26{u_2}^2 + 2.83{u_3}^2 - 10.6u_1u_2 - 3.2u_1u_3 - 12.7u_2u_3 \end{bmatrix}$$

$$\boldsymbol{B_2}(\boldsymbol{x}) \triangleq \begin{bmatrix} -2.86x + 2.34y + 16.8z & -2.56x - 1.23y - 20.2z & 1.59x - 1.16y + 3.61z \\ 2.76x + 0.356y - 9.28z & -2.98x + 3.22y - 12.9z & -0.129x - 4.02y + 19.9z \\ -4.72x + 3.42y + 2.26z & 5.47x + 3.28y + 1.58z & -1.06x - 6.62y + 4.49z \end{bmatrix}$$

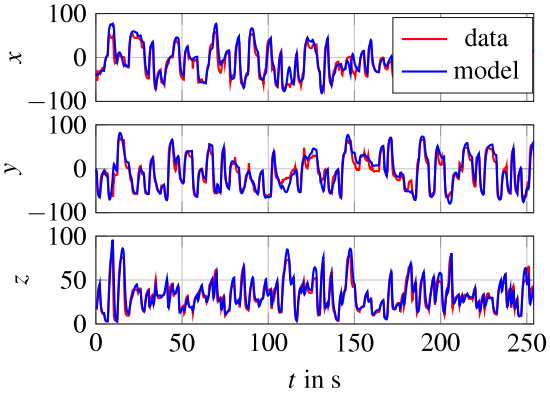

Fig. 4. Validation of the identified model: Comparison between measured end-effector coordinates (mm) in red and the model response in blue under the same input series. The individual fits were calculated as $\text{fit}_x = 83.7\%$, $\text{fit}_y = 85.1\%$, $\text{fit}_z = 94.7\%$. (For interpretation of the references to colour in this figure legend, the reader is referred to the web version of this article.)

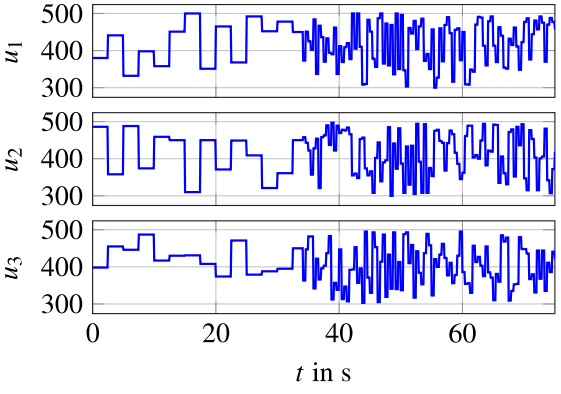

Fig. 5. Excitation inputs used for SINDYc.

This was done in order to capture as much of the dynamics as possible, i.e. slow and fast modes. Under these excitation conditions, the available training data could deliver a sufficiently general dynamical model of the robot, which nonetheless constitutes an approximation of an infinite-dimensional system. As such, it can never fully capture the exact dynamics of the system. Moreover, significant structural alterations in the robot configuration, such as using a different end-effector tool or mounting it on a different position of the link, will likely require new identification.

3. Robot control design

The control strategy for the positioning of the soft robot end-effector employs a cascaded architecture as show in Fig. 6. A STSMC generates

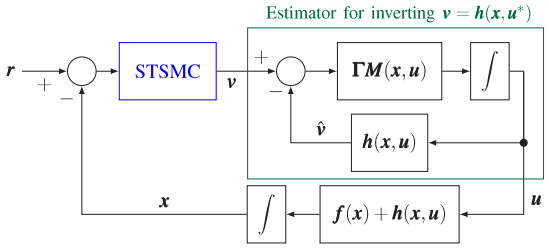

Fig. 6. Control architecture with the STSMC in cascade with the adaptive estimator (in green). The latter is used for inversion of the nonlinear mapping $\boldsymbol{v} = \boldsymbol{h}(\boldsymbol{x}, \boldsymbol{u}^*)$ with respect to the desired actuators output $\boldsymbol{u}^*$. (For interpretation of the references to colour in this figure legend, the reader is referred to the web version of this article.)

a "velocity" command $\boldsymbol{v}$, which has to be realised by an appropriate control input $\boldsymbol{u}^*$ such that $\boldsymbol{v} = \boldsymbol{h}(\boldsymbol{x}, \boldsymbol{u}^*)$ according to (4). An online estimator is then used to dynamically invert this nonlinear mapping and provide the necessary voltage input to the robot actuators.

3.1. Super twisting sliding-mode position control

Consider the virtual input $\boldsymbol{v} \triangleq \boldsymbol{h}(\boldsymbol{x}, \boldsymbol{u}^*)$ such that the system dynamics in (4) can be re-written as

$$\dot{\boldsymbol{x}} = \boldsymbol{f}(\boldsymbol{x}) + \boldsymbol{v} \, .$$

Then for a sufficiently smooth reference signal $\boldsymbol{r} = \begin{bmatrix} r_x & r_y & r_z \end{bmatrix}^T$, the dynamics of the position error $\boldsymbol{e} \triangleq \boldsymbol{x} - \boldsymbol{r} = \begin{bmatrix} e_x & e_y & e_z \end{bmatrix}^T$ reads

$$\dot{\boldsymbol{e}} = \boldsymbol{f}(\boldsymbol{x}) + \tilde{\boldsymbol{f}}(\boldsymbol{x}, \boldsymbol{u}^*) + \boldsymbol{v} - \dot{\boldsymbol{r}} \, ,$$

where $\tilde{\boldsymbol{f}} \triangleq \begin{bmatrix} \tilde{f}_x & \tilde{f}_y & \tilde{f}_z \end{bmatrix}^T$ is an unknown but bounded residual vector field due to modelling mismatch.

Define the *Sliding manifold* $S \triangleq \{\boldsymbol{x} \in \mathbb{R}^3 | \boldsymbol{e} = \boldsymbol{0}\}$. When the system is in sliding motion, i.e. the trajectories $\boldsymbol{e}(t)$ lie on S, the positioning error is zero. Select the control law

$$\boldsymbol{v} = \dot{\boldsymbol{r}} - \boldsymbol{f}(\boldsymbol{x}) - \underbrace{\left[k_{1,j} \lfloor e_j \rceil^{\frac{1}{2}} + k_{2,j} \int_0^t \text{sgn}(e_j(\tau)) d\tau \right]_j}_{\boldsymbol{v_{SMC}} \in \mathbb{R}^3 \text{ is a } 3\times1 \text{ vector with } j \in \{x,y,z\}} \tag{5}$$

where $\lfloor w \rceil^{\frac{1}{2}} \triangleq |w|^{\frac{1}{2}} \text{sgn}(w)$ and $\text{sgn}(\cdot)$ is the signum function defined by

$$\text{sgn}(w) \triangleq \begin{cases} \dfrac{w}{|w|} & , \text{for } w \neq 0 \\ \omega \in [-1, 1] & , \text{for } w = 0 \end{cases} .$$

Assuming for now that any control demand $\boldsymbol{v}$ can be realised by the actuators signals $\boldsymbol{u}$, leads to the following closed-loop error dynamics

$$\dot{\boldsymbol{e}} = \tilde{\boldsymbol{f}}(\boldsymbol{x}, \boldsymbol{u}^*) + \boldsymbol{v_{SMC}}. \tag{6}$$

Assumption 1 (*Bounded-Rate Perturbations*)**.** There exist finite constants $\Delta_x, \Delta_y, \Delta_z > 0$ such that

$$\left| \dot{\tilde{f}}_x(\boldsymbol{x}, \boldsymbol{u}) \right| < \Delta_x \, , \quad \left| \dot{\tilde{f}}_y(\boldsymbol{x}, \boldsymbol{u}) \right| < \Delta_y \, , \quad \left| \dot{\tilde{f}}_z(\boldsymbol{x}, \boldsymbol{u}) \right| < \Delta_z$$

$\forall(\boldsymbol{x},\boldsymbol{u}) \in \mathscr{W} \times \mathscr{U}$.

The foregoing assumption is not overly conservative in physical systems since it merely states that the perturbations induced by model uncertainty and input cross-couplings do not grow in amplitude at infinite rates. Under Assumption 1, selecting the controller gains as

$$k_{2,x} > \Delta_x,\ k_{2,y} > \Delta_y,\ k_{2,z} > \Delta_z,\ k_{1,x} \geq 1.8\sqrt{k_{2,x}+\Delta_x}$$
$$k_{1,y} \geq 1.8\sqrt{k_{2,y}+\Delta_y},\ k_{1,z} \geq 1.8\sqrt{k_{2,z}+\Delta_z}$$

ensures finite-time stability of the origin (Moreno & Osorio, 2012). As it can be seen from the tuning of the control gains, it is essential that the bounds $\Delta_x, \Delta_y, \Delta_z$ be not overly conservative otherwise this could lead to excessive control action. A good starting point to this end is to compute the difference

$$\begin{bmatrix}\tilde{f}_x\\ \tilde{f}_y\\ \tilde{f}_z\end{bmatrix} = \underbrace{\dot{\boldsymbol{x}}}_{\text{Data}} - \underbrace{[\boldsymbol{f}(\boldsymbol{x},\boldsymbol{u}) + \boldsymbol{h}(\boldsymbol{x},\boldsymbol{u})]}_{\text{SINDYc Model}}$$

and the associated derivatives $\dot{\tilde{f}}_x(\boldsymbol{x},\boldsymbol{u}), \dot{\tilde{f}}_y(\boldsymbol{x},\boldsymbol{u}), \dot{\tilde{f}}_z(\boldsymbol{x},\boldsymbol{u})$. Note that $\dot{\boldsymbol{x}}$ was already numerically computed from measurement data during the identification phase. Then one can set $\Delta_j = \max_t |\dot{\tilde{f}}_j(\boldsymbol{x}(t),\boldsymbol{u}(t))|$, where $j \in \{x,y,z\}$ and $t \in [0, t_f]$ with t_f corresponding to the last collected sample. Finally, to alleviate the effect of chattering in the control signal, the discontinuous signum function is approximated by a continuous one defined as (Llibre, Novaes, & Teixeira, 2015)

$$\phi_\delta(q,\delta) \triangleq \begin{cases}\text{sgn}(q) & \text{if } |q| \geq \delta\\ \dfrac{q}{\delta} & \text{if } |q| < \delta\end{cases},$$

where $\delta > 0$. As a consequence of this approximation, the closed-loop system vector field is now continuous, at the cost however of a loss in accuracy. It was shown in Papageorgiou and Edwards (2022) that the closed-loop system trajectories converge to an ellipsoid containing the origin that can become arbitrarily small as $\delta \to 0$. This means that the regularised closed-loop system retains all of its robustness properties, while the trade-off is introduced only in terms of accuracy.

3.2. Input mapping inversion

As mentioned earlier in Section 3, it can be challenging, if at all possible, to obtain a closed-form expression for the inverse mapping $\boldsymbol{u}^* = \boldsymbol{h}^{-1}(\boldsymbol{x},\boldsymbol{v})$. An online estimator structure can be used instead to asymptotically estimate the input values $\boldsymbol{u}^*$ given the control command $\boldsymbol{v}$. Dynamic nonlinear mapping inversion using observers has been used in adaptive control and parameter monitoring problems in systems with nonlinear parametrisation (Grip, Johansen, Imsland, & Kaasa, 2010). For the soft robot system, the actuators signal $\boldsymbol{u}$ is an estimate of the ideal solution $\boldsymbol{u}^*$ given by

$$\dot{\boldsymbol{u}} = \text{Proj}\left[\boldsymbol{u}, \boldsymbol{\Gamma}\boldsymbol{M}(\boldsymbol{x},\boldsymbol{u})(\boldsymbol{v} - \boldsymbol{h}(\boldsymbol{x},\boldsymbol{u}))\right] \tag{7}$$

where $\boldsymbol{\Gamma}$ is a constant positive definite matrix and the matrix function $\boldsymbol{M}(\boldsymbol{x},\boldsymbol{u})$, bounded for bounded $\boldsymbol{x}$, is to be designed. The projection operator defined as (Krstic, Kanellakopoulos, & Kokotovic, 1995)

$$\text{Proj}[\boldsymbol{u},\boldsymbol{\tau}] = \begin{cases}\boldsymbol{\tau},\ P(\boldsymbol{u}) < 0 \text{ or } P(\boldsymbol{u}) \geq 0 & \& \nabla P^T\boldsymbol{\tau} \leq 0\\ \boldsymbol{\tau} - \frac{\nabla P}{\|\nabla P\|}\left\langle \frac{\nabla P}{\|\nabla P\|}, \boldsymbol{\tau}\right\rangle P(\boldsymbol{u}), & P(\boldsymbol{u}) \geq 0\\ & \& \nabla P^T\boldsymbol{\tau} > 0\end{cases}$$

and with the convex scalar function $P : \mathscr{W} \to \mathbb{R}$ given by

$$P(\boldsymbol{u}) = \epsilon(\boldsymbol{u}-\boldsymbol{p})^T\boldsymbol{Q}^{-1}(\boldsymbol{u}-\boldsymbol{p}) - 1,\ \epsilon > 1$$
$$\boldsymbol{p}^T = \frac{1}{2}\left[u_1^{min}+u_1^{max} \quad u_2^{min}+u_2^{max} \quad u_3^{min}+u_3^{max}\right],$$
$$\boldsymbol{Q} = \frac{1}{2}\begin{bmatrix}u_1^{max}-u_1^{min} & 0 & 0\\ 0 & u_2^{max}-u_2^{min} & 0\\ 0 & 0 & u_3^{max}-u_3^{min}\end{bmatrix}.$$

ensures that the estimated input vector $\boldsymbol{u}$ always remains in the compact set $\mathscr{U}$. Choosing $\epsilon > 1$ relates to the parameters $\boldsymbol{u}$ not being allowed to assume or exceed their extreme values, i.e. to being strictly inside the ellipsoid defined by $P(\boldsymbol{u}) = 0$.

It has been shown in Grip et al. (2010) that if there can be found a symmetric positive definite matrix function $\boldsymbol{\Sigma}(\boldsymbol{x})$, bounded for bounded $\boldsymbol{x}$, such that the conditions

$$\underbrace{\boldsymbol{M}(\boldsymbol{x},\boldsymbol{u}^*)\frac{\partial \boldsymbol{h}}{\partial \boldsymbol{u}}(\boldsymbol{x},\boldsymbol{u}) + \left(\frac{\partial \boldsymbol{h}}{\partial \boldsymbol{u}}(\boldsymbol{x},\boldsymbol{u})\right)^T\boldsymbol{M}^T(\boldsymbol{x},\boldsymbol{u}^*)}_{2\boldsymbol{H}(\boldsymbol{x},\boldsymbol{u}^*,\boldsymbol{u})} \geq 2\boldsymbol{\Sigma}(\boldsymbol{x}) \tag{8}$$

$$\left\|\boldsymbol{h}(\boldsymbol{x},\boldsymbol{u}^*) - \boldsymbol{h}(\boldsymbol{x},\boldsymbol{u})\right\| \leq L\sqrt{\tilde{\boldsymbol{u}}^T\boldsymbol{\Sigma}(\boldsymbol{x})\tilde{\boldsymbol{u}}},\ L > 0 \tag{9}$$

$$\exists T, \alpha_0 > 0,\ :\ \int_t^{t+T}\boldsymbol{\Sigma}(\boldsymbol{x}(\tau))d\tau \geq \alpha_0\boldsymbol{I} \tag{10}$$

hold for all pairs $(\boldsymbol{u}^*,\boldsymbol{u})$, then the estimation error $\tilde{\boldsymbol{u}} \triangleq \boldsymbol{u}^* - \boldsymbol{u}$ converges to the origin exponentially fast. Selecting

$$\boldsymbol{M}(\boldsymbol{x},\boldsymbol{u}) = \left(\frac{\partial \boldsymbol{h}}{\partial \boldsymbol{u}}(\boldsymbol{x},\boldsymbol{u})\right)^T \tag{11}$$

renders $\boldsymbol{H}$ symmetric and therefore diagonalisable. Then

$$\boldsymbol{H}(\boldsymbol{x},\boldsymbol{u}^*,\boldsymbol{u}) \geq \inf_{(\boldsymbol{u}^*,\boldsymbol{u})\in\mathscr{U}\times\mathscr{U}}\lambda_{min}\left(\boldsymbol{H}(\boldsymbol{x},\boldsymbol{u}^*,\boldsymbol{u})\right)\boldsymbol{I},$$

where $\lambda_{min}(\cdot)$ denotes that smallest eigenvalue of a matrix. This implies that condition (8) is satisfied with

$$\boldsymbol{\Sigma}(\boldsymbol{x}) = \inf_{(\boldsymbol{u}^*,\boldsymbol{u})\in\mathscr{U}\times\mathscr{U}}\lambda_{min}\left(\boldsymbol{H}(\boldsymbol{x},\boldsymbol{u}^*,\boldsymbol{u})\right)\boldsymbol{I}$$

whenever $\boldsymbol{H}$ is positive definite. Under the same assumption and due to the Lipschitz continuity of $\boldsymbol{h}$ ($\|\partial\boldsymbol{h}/\partial\boldsymbol{u}\|$ is bounded for bounded inputs and states), it is easy to show that condition (9) is also satisfied since $\exists L_0 > 0$ such that

$$\left\|\boldsymbol{h}(\boldsymbol{x},\boldsymbol{u}^*) - \boldsymbol{h}(\boldsymbol{x},\boldsymbol{u})\right\| \leq L_0\|\tilde{\boldsymbol{u}}\|$$
$$\leq \underbrace{\frac{L_0}{\sqrt{\inf_{\boldsymbol{x}\in\mathscr{W}}\lambda_{min}(\boldsymbol{\Sigma}(\boldsymbol{x}))}}}_{L}\sqrt{\boldsymbol{u}^T\inf_{\boldsymbol{x}\in\mathscr{W}}\lambda_{min}(\boldsymbol{\Sigma}(\boldsymbol{x}))\boldsymbol{u}}$$
$$\leq L\sqrt{\tilde{\boldsymbol{u}}^T\boldsymbol{\Sigma}(\boldsymbol{x})\tilde{\boldsymbol{u}}}.$$

Since $\mathscr{W}$ is compact, the infimum of $\lambda_{min}(\boldsymbol{\Sigma}(\boldsymbol{x}))$ over $\mathscr{W}$ always exist and it is positive whenever $\boldsymbol{H}$ is positive definite. Finally, condition (10) expresses the standard requirement for persistence of excitation, which in this problem can be interpreted as a requirement for sufficient control demand $\boldsymbol{v}$.

Remark 2. Proving the validity of (8) analytically can be very challenging or even impossible given the complexity of $\boldsymbol{h}$. Numerical assessment can be employed instead, where $\lambda_{min}(\boldsymbol{H})$ is calculated over a subset of the state-space within $\mathscr{W}$ and for a number of pairs $(\boldsymbol{u},\boldsymbol{u}^*) \in \mathscr{U}\times\mathscr{U}$. These pairs can be generated by setting $\boldsymbol{u}$ equal to the estimated input and then assigning variations over a range (e.g. ±20%) to $\boldsymbol{u}^*$. Figs. 7–9 illustrate such an evaluation for the soft robot in this study for input variations up to ±50% (along with the reference trajectories that were used in teh experimental evaluation of the method). Specifically, for each collected data point (x,y,z,u_1,u_2,u_3) in Fig. 2, triplets $(\bar{u}_1,\bar{u}_2,\bar{u}_3)$ generated by varying either of (u_1,u_2,u_3) by up to ±50% are used for calculating the minimum eigenvalue of $\boldsymbol{H}$. If for any of these 9-tuples $(\boldsymbol{x},\boldsymbol{u},\bar{\boldsymbol{u}}) = (x,y,z,u_1,u_2,u_3,\bar{u}_1,\bar{u}_2,\bar{u}_3)$ it holds that $\lambda_{min}(\boldsymbol{H}) \leq 0$, then condition (8) is not satisfied and the associated point (x,y,z) is coloured red, otherwise is coloured blue. This mostly occurs close to the boundaries of the workspace and for the largest difference between $\boldsymbol{u}$ and $\boldsymbol{u}^*$ (worst case of estimation). In such cases asymptotic estimation of $\boldsymbol{u}^*$ is not guaranteed and additional logic can be implemented to pause the estimation until $\boldsymbol{H}$ is again positive definite. In any case, the projection of the estimation law ensures boundedness of the estimation error $\tilde{\boldsymbol{u}}$.

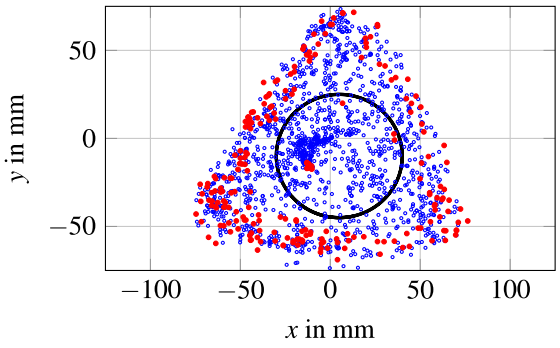

Fig. 7. Top view of workspace (blue points) with reference trajectory (black circle). The red points show where condition (8) does not hold. (For interpretation of the references to colour in this figure legend, the reader is referred to the web version of this article.)

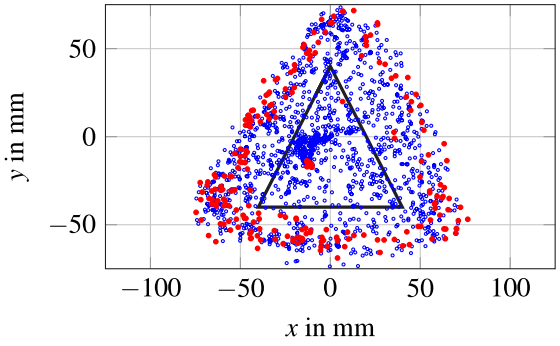

Fig. 8. Top view of workspace (blue points) with reference trajectory (black triangle). The red points show where condition (8) does not hold. (For interpretation of the references to colour in this figure legend, the reader is referred to the web version of this article.)

3.3. Stability analysis

The closed-loop dynamics of the robot end-effector position error with the input estimator included is written as

$$\dot{\boldsymbol{e}} = \tilde{\boldsymbol{f}}(\boldsymbol{x},\boldsymbol{u}) + \boldsymbol{v}_{\boldsymbol{SMC}} + \tilde{\boldsymbol{h}}(\boldsymbol{x},\boldsymbol{u}^* - \tilde{\boldsymbol{u}}) \tag{12}$$

where the control command error

$$\tilde{\boldsymbol{h}} \triangleq \boldsymbol{v} - \boldsymbol{h}(\boldsymbol{x},\boldsymbol{u}^* - \tilde{\boldsymbol{u}}) = \boldsymbol{h}(\boldsymbol{x},\boldsymbol{u}^*) - \boldsymbol{h}(\boldsymbol{x},\boldsymbol{u}^* - \tilde{\boldsymbol{u}}) \tag{13}$$

converges to $\mathbf{0}$ exponentially, when conditions (8)–(10) hold and is bounded otherwise.

Proposition 1 (*Stability of Closed-Loop Error Dynamics*). *Consider the closed-loop positioning error dynamics for the soft robot system under the control law (5). If conditions (8)–(10) hold and under Assumption 1, the origin is a Uniformly Globally Asymptotically Stable (UGAS) equilibrium point of the closed-loop system.*

Proof. The proof is detailed in Appendix. □

Remark 3. The Uniformly Globally Bounded (UGB) property of (A.1b) due to the projector operator satisfies Assumption 6 in Loría (2008) and further implies that $\left|\frac{\partial V}{\partial \zeta}\boldsymbol{g}_{\zeta}(t,\boldsymbol{\zeta},\tilde{\boldsymbol{u}})\right| \leq |\boldsymbol{P}|L_u\|\boldsymbol{\zeta}\|\tilde{U}$, where $\tilde{U}$ is an upper bound for $\|\tilde{\boldsymbol{u}}\|$. Then, $\frac{\partial V}{\partial \zeta}\boldsymbol{g}_{\zeta}(t,\boldsymbol{\zeta},\tilde{\boldsymbol{u}}) = o(W(\boldsymbol{\zeta}))$, with W defined earlier. By Theorem 1 in Loría (2008), the solutions of (A.1) are UGB *even if conditions (8)–(10) do not hold.*

Remark 4. When the conditions in Proposition 1 do not hold, $\tilde{\boldsymbol{h}}$ can be lumped to the existing bounded-rate perturbation in the system.

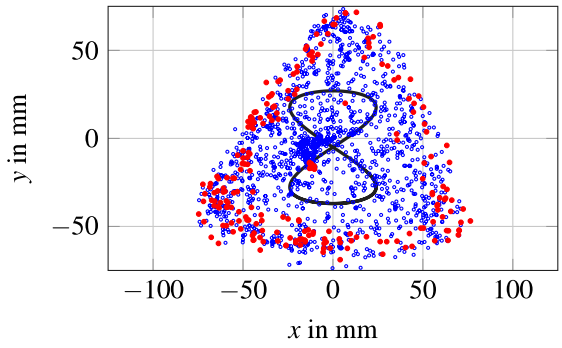

Fig. 9. Top view of workspace (blue points) with reference trajectory (black infinity sign). The red points show where condition (8) does not hold. (For interpretation of the references to colour in this figure legend, the reader is referred to the web version of this article.)

The STSMC gains will then need to be adjusted accordingly. When the finite-time conditions do not hold, $e(t)$ will temporarily leave the sliding manifold until the controller gains exceed the perturbation rate again.

4. Experimental results

4.1. Test scenarios and benchmark controller

The proposed end-effector positioning solution was experimentally tested on the soft robot system in three different scenarios:

1. Circular trajectory of radius equal to 35 mm with centre at $(5,-10,30)$ mm.
2. Triangular trajectory defined by the points $A(-40,-40,20)$, $B(0,40,20)$ and $C(40,-40,20)$ (in mm).
3. Infinity-sign trajectory centred at $(0,-5,5)$ mm.

A decoupled PI control scheme was also implemented on the soft robot system for a benchmark comparison.

The controller had the form

$$\boldsymbol{v}_{\boldsymbol{PI}} = \dot{\boldsymbol{r}} - \boldsymbol{f}(\boldsymbol{x}) - \begin{bmatrix} K_{P,x}\left(e_x - \frac{1}{\tau_{I,x}}\int_0^t e_x(\tau)d\tau\right) \\ K_{P,y}\left(e_y - \frac{1}{\tau_{I,y}}\int_0^t e_y(\tau)d\tau\right) \\ K_{P,z}\left(e_z - \frac{1}{\tau_{I,z}}\int_0^t e_z(\tau)d\tau\right) \end{bmatrix}$$

Table 2 shows the scheme's parameters. The tuning of the PI was done based on the Ziegler–Nichols method. The MAE and RMSE were used for comparing the closed-loop system performance for the STSMC and PI.

Remark 5. It should be noted that the PI scheme also employed the input mapping inversion block as well as the feedback linearising term $-\boldsymbol{f}(\boldsymbol{x})$ to cancel known nonlinearities. This, in essence, rendered the closed-loop system a perturbed integrator and therefore, the controller was abled to be tuned via Ziegler–Nichols rules to obtain the (heuristically) best gains possible.

4.2. Results

Table 3 shows the MAE and RMSE values for the tracking of the circular, triangular and infinity-sign end-effector position profiles shown in Figs. 11–13, respectively. As it can be seen, for the triangular reference signal both controllers have similar performance. This is expected, since the desired trajectory comprises segments of linear motion at constant speeds. However, in the case of circular and infinity-sign profiles, the STSMC outperforms the PI with the latter having

Table 2
Controllers and estimator gains and parameters.

Symbol	Value
STSMC parameters	
$(k_{1,x}, k_{1,y}, k_{1,z})$	(10, 10, 10)
$(k_{2,x}, k_{2,y}, k_{2,z})$	(10, 10, 10)
δ	3 (mm)
Estimator parameters	
$u_i^{min},\ i = 1, 2, 3$	300 (digital signal)
$u_i^{max},\ i = 1, 2, 3$	500 (digital signal)
ϵ	1.1
$\boldsymbol{\Gamma}$	$\begin{bmatrix} 30 & 0 & 0 \\ 0 & 30 & 0 \\ 0 & 0 & 30 \end{bmatrix}$
PIs parameters	
$(K_{P,x}, K_{P,y}, K_{P,z})$	(3.24, 2.21, 1.08)
$(\tau_{I,x}, \tau_{I,y}, \tau_{I,z})$	(2.23, 2.15, 1.67)

Table 3
MAE and RMSE in mm for the PI and the STSMC for all three scenarios.

		MAE (x, y, z)	RMSE (x, y, z)
Circle	PI	13.24, 8.43, 5.22	2.31, 2.29, 1.23
	STSMC	3.87, 2.42, 2.37	0.94, 0.88, 0.77
Triangle	PI	8.47, 4.51, 3.33	1.43, 1.57, 1.18
	STSMC	4.42, 8.55, 4.55	1.01, 1.40, 1.22
Infinity	PI	36.74, 19.97, 33.39	5.85, 5.33, 11.97
	STSMC	12.84, 13.48, 6.30	2.89, 2.97, 2.46

up to five times larger MAE and four times larger RMSE, especially in the z-coordinate. This can be clearly seen in Figs. 14–16, which illustrate the position error signals for both control schemes for all three scenarios. Specifically in the case of the circular trajectory, the proposed control solution delivers positioning accuracy of approximately 3 mm corresponding to 8.5% of the radius of the circle. This level of accuracy is sufficient for demonstrating the feasibility of the proposed approach. Finally, the performance of the online input estimator is shown in Figs. 17–19, where the control command $\boldsymbol{v} = \boldsymbol{h}(\boldsymbol{x}, \boldsymbol{u}^*)$ is plotted together with the actual control input $\boldsymbol{h}(\boldsymbol{x}, \boldsymbol{u})$ for the three scenarios. The estimator generates sufficiently accurate values for the actuator signals $\boldsymbol{u}$ except for some isolated cases when the projection operation is activated. This occurs when the control demand is very close to the boundary of the set $\mathcal{U}$ or outside of it.

5. Conclusions and future work

This study proposed a framework for nonlinear model-based control of soft robots with application to a single-link continuum manipulator. The dynamics of the system was mathematically described by employing physics-informed sparse nonlinear regression with control. The obtained model, although heavily nonlinear, had only three states all of which were observable. This was a direct consequence of the utilised identification methodology. This low-dimensionality facilitated the design of a STSMC that was used for the positioning of the robot end-effector. An online estimator was employed for inverting the nonlinear mapping between control command and actuation signals. The stability of the closed-loop system was analysed and finally, the applicability of the proposed solution was demonstrated with experiments on a real soft robotic platform.

The proposed framework features a modular architecture that covers both the modelling and the control parts. This implies that an alternative identification method can be used instead of SINDYc. Depending on the extent of structural variations (e.g. relative degree, dimension, observability, etc.) of the different models, several modifications may be needed in the control design, especially in connection to the input mapping inversion. Nonetheless, the same steps presented in this paper can be followed for obtaining the complete control solution.

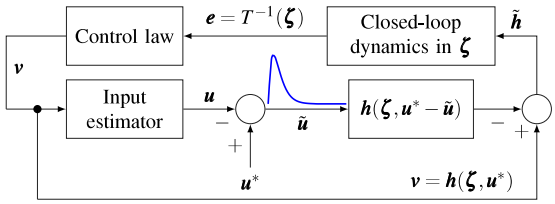

Fig. 10. Closed-loop system as a feedback interconnection of the two error subsystems (Σ_1) and (Σ_2).

The verification of condition (8) that guarantees inversion of the nonlinear input mapping was numerically assessed in the current manuscript. Although boundedness of the solutions are ensured even if the condition is violated, there is not any performance guarantee in terms of absolute accuracy in such a case. This could potentially be amended by constraining the controller output $\boldsymbol{v}$ in the set where the input mapping is always invertible.

The selection of the STSMC was made on the basis of its strong robustness against non-parametric perturbations. This is very helpful in the design when dealing with cross-couplings and model uncertainties. However, the STSMC does not explicitly account for constraints apart from the control error. This is a limitation of the specific control choice compared to e.g. SINDy-MPC when hard constraints are imposed in the problem formulation. An extension to the proposed scheme will include the addition of adaptive features to the STSMC that can handle performance constraints. More specifically, future work will pursue the integration of learning-based feed-forward components to the existing scheme. Such combination will maintain the stability of the closed-loop system while facilitating the exploration of the behaviour of the robot during the execution of complex tasks that impose constraints (e.g., interactions with the environment or humans). Furthermore, the learning strategy will be useful such as in the presence of structural changes in the robot configuration (e.g. different gripper or location of the tool, extra links etc.) that will severely change the dynamical properties of the system, thus compromising the accuracy of the base model.

Comparative analysis of different control schemes and input estimators in the context of the proposed framework will also be pursued in future work.

Declaration of competing interest

The authors declare that they have no known competing financial interests or personal relationships that could have appeared to influence the work reported in this paper.

Appendix. Proof of Proposition 1

The closed-loop system in (12) can be viewed as the feedback interconnection of two subsystems: the finite-time stable dynamics of the unperturbed closed-loop system in (6) and the exponentially stable dynamics of the control command error $\tilde{\boldsymbol{h}}$ defined in (13) (Fig. 10). The finite-time stability of the origin of (6) implies the existence of a local diffeomorphism $\boldsymbol{\zeta} = \boldsymbol{T}(\boldsymbol{e})$ and a positive definite absolutely continuous quadratic Lyapunov function $V = \boldsymbol{\zeta}^T \boldsymbol{P} \boldsymbol{\zeta}$ such that $\dot{V} \leq -c\|\boldsymbol{\zeta}\|,\ c > 0$ (Moreno & Osorio, 2012). Under this coordinate transformation, the feedback interconnected systems can be re-written as

$$(\Sigma_1) : \dot{\boldsymbol{\zeta}} = \boldsymbol{f}_{\boldsymbol{\zeta}}(t, \boldsymbol{\zeta}) + \boldsymbol{g}_{\boldsymbol{\zeta}}(t, \boldsymbol{\zeta}, \tilde{\boldsymbol{u}}) \tag{A.1a}$$

$$(\Sigma_2) : \dot{\tilde{\boldsymbol{u}}} = \boldsymbol{f}_{\tilde{\boldsymbol{u}}}(t, \boldsymbol{\zeta}, \tilde{\boldsymbol{u}})\ , \text{ where} \tag{A.1b}$$

$$\boldsymbol{f}_{\boldsymbol{\zeta}}(t, \boldsymbol{\zeta}) \triangleq \frac{\partial \boldsymbol{T}}{\partial \boldsymbol{e}} \left[\tilde{\boldsymbol{f}}(\boldsymbol{x}, \boldsymbol{u}) + \boldsymbol{v}_{SMC}(\boldsymbol{T}^{-1}(\boldsymbol{\zeta})) \right]$$

$$\boldsymbol{g}_{\boldsymbol{\zeta}}(t, \boldsymbol{\zeta}, \tilde{\boldsymbol{u}}) \triangleq \frac{\partial \boldsymbol{T}}{\partial \boldsymbol{e}} \tilde{\boldsymbol{h}} \left(\boldsymbol{r} + \boldsymbol{T}^{-1}(\boldsymbol{\zeta}), \boldsymbol{u}^* - \tilde{\boldsymbol{u}} \right)$$

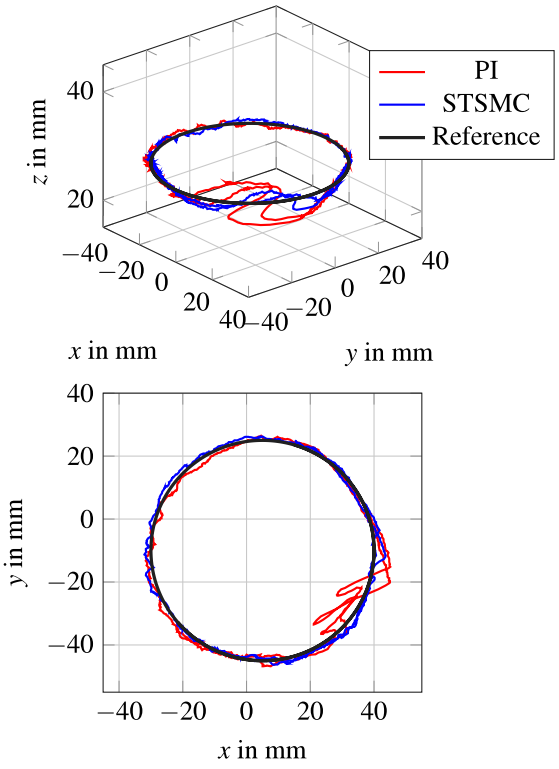

Fig. 11. Perspective and top view of tracking of the circular motion profile (black). The performance of the STSMC (blue) is superior to that of the PI-based (red) solution. (For interpretation of the references to colour in this figure legend, the reader is referred to the web version of this article.)

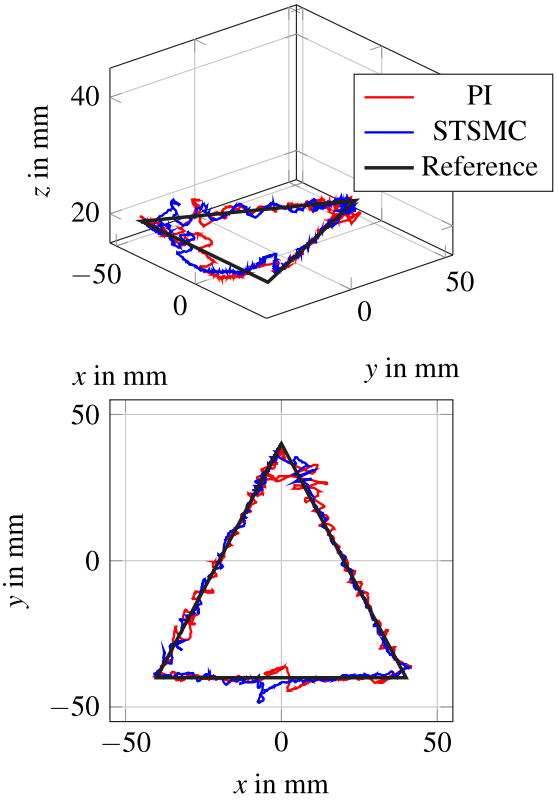

Fig. 12. Perspective and top view of tracking of the triangular motion profile (black). The performance of the STSMC (blue) is superior to that of the PI-based (red) solution. (For interpretation of the references to colour in this figure legend, the reader is referred to the web version of this article.)

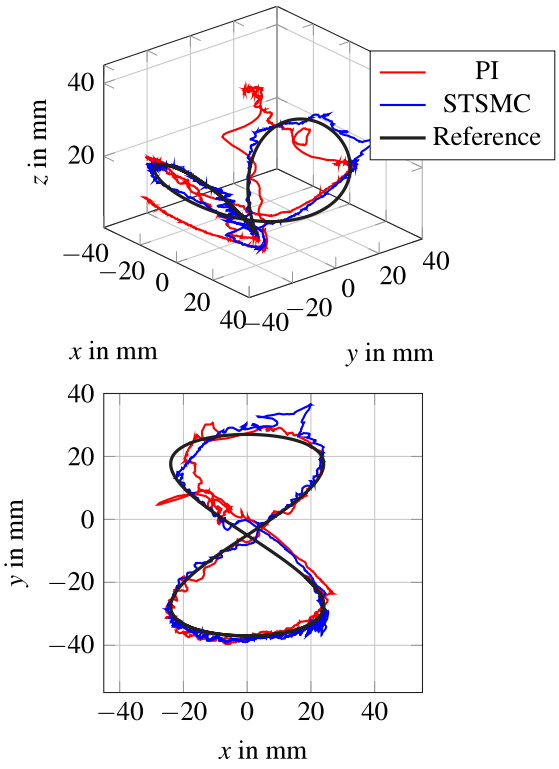

Fig. 13. Perspective and top view of tracking of the infinity sign motion profile (black). The performance of the STSMC (blue) is superior to that of the PI-based (red) solution. (For interpretation of the references to colour in this figure legend, the reader is referred to the web version of this article.)

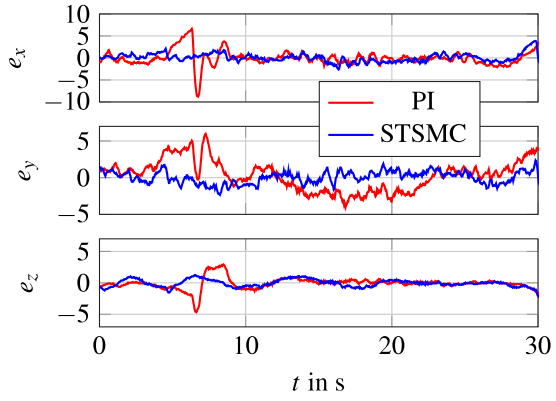

Fig. 14. Circle: End-effector position errors $e_x = x - r_x$, $e_y = y - r_y$, $e_z = z - r_z$ in mm for the STSMC (blue) and PI (red) case. (For interpretation of the references to colour in this figure legend, the reader is referred to the web version of this article.)

$$\boldsymbol{f}_{\tilde{\boldsymbol{u}}}(t,\boldsymbol{\zeta},\tilde{\boldsymbol{u}}) \triangleq -\mathrm{Proj}\left[\boldsymbol{u}, \boldsymbol{\Gamma}\boldsymbol{M}(\boldsymbol{r}+\boldsymbol{T}^{-1}(\boldsymbol{\zeta}),\boldsymbol{u}^*-\tilde{\boldsymbol{u}}) \cdot \left(\boldsymbol{v}-\boldsymbol{h}(\boldsymbol{r}+\boldsymbol{T}^{-1}(\boldsymbol{\zeta}),\boldsymbol{u}^*-\tilde{\boldsymbol{u}})\right)\right]$$

The feedback system (A.1a)–(A.1b) can be viewed as a *cascaded* interconnection, where the solutions $\tilde{\boldsymbol{u}}(t)$ of Σ_2 depend on the *parameter* $\boldsymbol{\zeta} = \boldsymbol{\zeta}(t)$ (Loría, 2008). Showing that the origin of (Σ_1)-(Σ_2) is UGAS amounts to satisfying Assumptions 1,4,5,7 and the conditions of Theorem 2 in Loría (2008).

Assumptions 1 and 5 (UGAS of (Σ_1) with $\boldsymbol{g}_{\boldsymbol{\zeta}} \equiv \boldsymbol{0}$) are implied by the finite-time stability of (6). Assumption 4 requires the existence of a $\mathscr{C}_1$ positive-definite, radially unbounded function $V_1(t,\boldsymbol{\zeta})$, a class $\mathscr{K}_\infty$ function α_1 and two continuous, positive non-decreasing functions

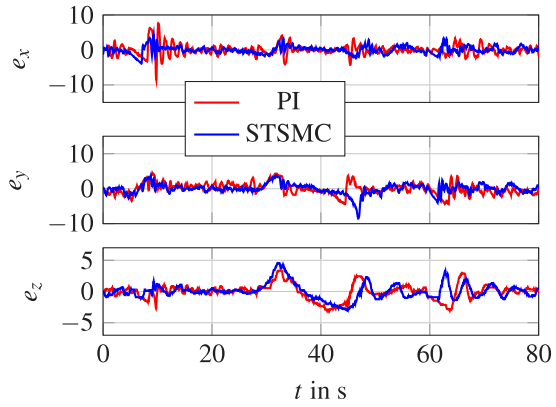

Fig. 15. Triangle: End-effector position errors $e_x = x - r_x$, $e_y = y - r_y$, $e_z = z - r_z$ in mm for the STSMC (blue) and PI (red) case. (For interpretation of the references to colour in this figure legend, the reader is referred to the web version of this article.)

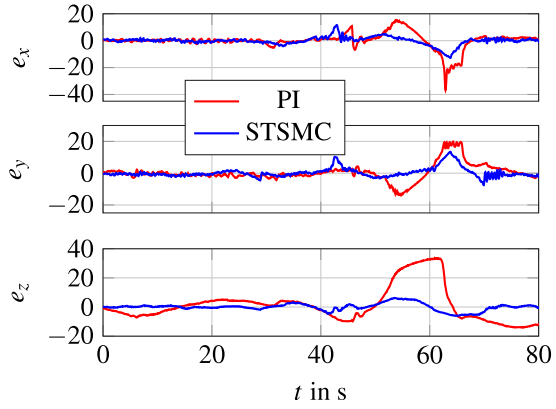

Fig. 16. Infinity sign: End-effector position errors $e_x = x - r_x$, $e_y = y - r_y$,. $e_z = z - r_z$ in mm for the STSMC (blue) and PI (red) case. (For interpretation of the references to colour in this figure legend, the reader is referred to the web version of this article.)

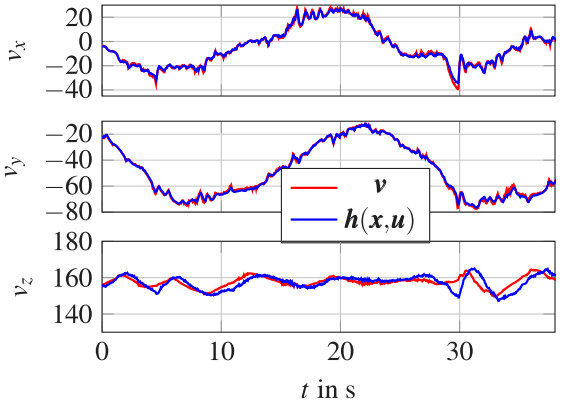

Fig. 17. Circle: Commanded (red) and actual (blue) control input for the STSMC. (For interpretation of the references to colour in this figure legend, the reader is referred to the web version of this article.)

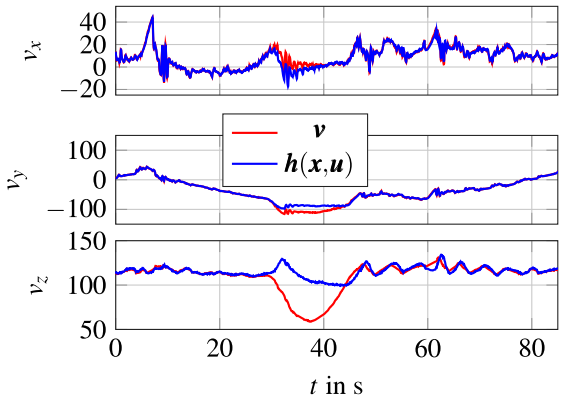

Fig. 18. Triangle: Commanded (red) and actual (blue) control input for the STSMC. (For interpretation of the references to colour in this figure legend, the reader is referred to the web version of this article.)

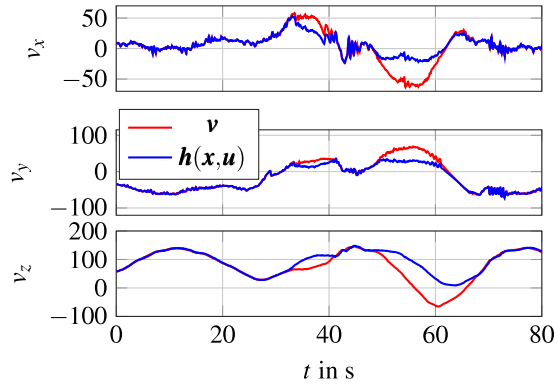

Fig. 19. Infinity sign: Commanded (red) and actual (blue) control input for the STSMC. (For interpretation of the references to colour in this figure legend, the reader is referred to the web version of this article.)

α_4, α_4' such that

$V_1(t,\zeta) \geq \alpha_1(\|\zeta\|)$

$\dot{V}_1(t,\zeta) \leq \alpha_4(\|\zeta\|)\alpha_4'(\|\tilde{u}\|)$ and

$$\int_{V_{1,0}}^{\infty} \frac{d\upsilon}{\alpha_4(\alpha_1^{-1}(\upsilon))} = \infty,$$

where $V_{1,0} > 0$ is a lower bound for V_1. Selecting $V_1 \triangleq V$, $\alpha_1 \triangleq \lambda_{min}(\boldsymbol{P})\|\zeta\|^2$ and considering the Lipschitz continuity of $\boldsymbol{h}$, Assumption 4 is satisfied with $\alpha_4(\|\zeta\|) \triangleq \|\zeta\|$ and $\alpha_4'(\|\tilde{u}\|) \triangleq 2\lambda_{max}(\boldsymbol{P})L_u\|\tilde{u}\|$, where $L_u > 0$ is larger or equal to the Lipschitz constant of $\boldsymbol{h}$. Indeed, taking the time derivative of V_1 along the trajectories of (Σ_1) gives:

$$\begin{aligned}\dot{V}_1(t,\zeta) &= 2\zeta^T \boldsymbol{P}\dot{\zeta} = 2\zeta^T \boldsymbol{P} f_\zeta(t,\zeta) + 2\zeta^T \boldsymbol{P} g_\zeta(t,\zeta,\tilde{u}) \\ &\leq -c\|\zeta\| + 2\|\zeta\| \cdot \lambda_{max}(\boldsymbol{P}) \cdot \|g_\zeta(t,\zeta,\tilde{u})\| \\ &\leq 2\|\zeta\| \cdot \lambda_{max}(\boldsymbol{P})L_u \cdot \|\tilde{u}\| = \alpha_4(\|\zeta\|)\alpha_4'(\|\tilde{u}\|)\end{aligned}$$

Assumption 7 requires asymptotic convergence of the solutions of (Σ_2) to the origin. This follows from the exponential stability of (A.1b) under the conditions (8)–(10).

Assumptions 1, 4, 5 and 7 constitute the first condition of Theorem 2 in Loría (2008), which states that the solutions of (A.1) are UGB. Satisfying the second condition of Theorem 2 requires that for the quadratic Lyapunov function V associated to (6) there exist class $\mathcal{K}$ functions α_5 and α_5' with

$$\left|\frac{\partial V}{\partial \zeta} g_\zeta(t,\zeta,\tilde{u})\right| \leq \alpha_5(\|\zeta\|)\alpha_5'(\|\tilde{u}\|)$$

and also, for each positive upper bound ρ for the solutions of (A.1b) $\exists \lambda_\rho, \eta_\rho > 0$ such that

$t \geq 0,\ \|\zeta\| \geq \eta_\rho \Rightarrow \alpha_5(\|\zeta\|) \leq \lambda_\rho W(\zeta),$

where W is a positive semi-definite function. Selecting $W(\zeta) \triangleq \|\zeta\|^2$ and using the same Lipschitz arguments as in the validation of Assumption 4, one can show that Theorem 2 is satisfied with $\alpha_5(\|\zeta\|) \triangleq$

$2|\boldsymbol{P}|L_u\|\zeta\|$, $\alpha_5'(\|\tilde{\boldsymbol{u}}\|) \triangleq \|\tilde{\boldsymbol{u}}\|$ and $\eta_r \triangleq \frac{2|\boldsymbol{P}|L_u}{\lambda_\rho}$, $\lambda_\rho > 0$ and $\forall \rho > 0$. Then by Proposition 2 in Loría (2008), the origin of (A.1) is UGAS. This completes the proof.

References

Bhattacharya, D., Cheng, L. K., & Xu, W. (2019). Sparse machine learning discovery of dynamic differential equation of an esophageal swallowing robot. *IEEE Transactions on Industrial Electronics*, *67*(6), 4711–4720.

Bhattacharya, D., Hashem, R., Cheng, L. K., & Xu, W. (2021). Nonlinear model predictive control of a robotic soft esophagus. *IEEE Transactions on Industrial Electronics*, *69*(10), 10363–10373.

Boiko, I., Fridman, L., Pisano, A., & Usai, E. (2007). Analysis of chattering in systems with second-order sliding modes. *IEEE transactions on Automatic control*, *52*(11), 2085–2102.

Bruder, D., Remy, C. D., & Vasudevan, R. (2019). Nonlinear system identification of soft robot dynamics using Koopman operator theory. In *2019 international conference on robotics and automation* (pp. 6244–6250). IEEE.

Brunton, S. L., Proctor, J. L., & Kutz, J. N. (2016a). Discovering governing equations from data by sparse identification of nonlinear dynamical systems. *Proceedings of the National Academy of Sciences*, *113*(15), 3932–3937.

Brunton, S. L., Proctor, J. L., & Kutz, J. N. (2016b). Sparse identification of nonlinear dynamics with control (SINDYc). *IFAC-PapersOnLine*, *49*(18), 710–715.

Cianchetti, M., Laschi, C., Menciassi, A., & Dario, P. (2018). Biomedical applications of soft robotics. *Nature Reviews Materials*, *3*(6), 143–153.

Della Santina, C., Duriez, C., & Rus, D. (2021). Model based control of soft robots: A survey of the state of the art and open challenges. arXiv preprint arXiv:2110.01358.

Emelyanov, S. V. (1967). *Variable structure control systems*. Moscow: Nouka.

Falkenhahn, V., Mahl, T., Hildebrandt, A., Neumann, R., & Sawodny, O. (2014). Dynamic modeling of constant curvature continuum robots using the Euler-Lagrange formalism. In *2014 IEEE/RSJ international conference on intelligent robots and systems* (pp. 2428–2433). IEEE.

Grip, H. F., Johansen, T. A., Imsland, L., & Kaasa, G.-o. (2010). Parameter estimation and compensation in systems with nonlinearly parameterized perturbations. *Automatica*, *46*(1), 19–28. http://dx.doi.org/10.1016/j.automatica.2009.10.013.

Jiang, H., Wang, Z., Liu, X., Chen, X., Jin, Y., You, X., et al. (2017). A two-level approach for solving the inverse kinematics of an extensible soft arm considering viscoelastic behavior. In *2017 IEEE international conference on robotics and automation* (pp. 6127–6133). IEEE.

Kaiser, E., Kutz, J. N., & Brunton, S. L. (2018). Sparse identification of nonlinear dynamics for model predictive control in the low-data limit. *Proceedings of the Royal Society of London, Series A (Mathematical and Physical Sciences)*, *474*(2219), Article 20180335.

Kim, D., Kim, S.-H., Kim, T., Kang, B. B., Lee, M., Park, W., et al. (2021). Review of machine learning methods in soft robotics. *PLoS One*, *16*(2), Article e0246102.

Krstic, M., Kanellakopoulos, I., & Kokotovic, P. V. (1995). *Nonlinear and adaptive control design* (first ed.). Wiley-Interscience.

Levant, A. (1993). Sliding order and sliding accuracy in sliding mode control. *International Journal of Control*, *58*(6), 1247–1263.

Li, J., Wang, H., & Zhu, J. (2022). Modeling of viscoelastic dielectric elastomer actuators based on the sparse identification method. In *2022 international conference on robotics and automation* (pp. 3252–3258). IEEE.

Lipson, H. (2014). Challenges and opportunities for design, simulation, and fabrication of soft robots. *Soft Robotics*, *1*(1), 21–27.

Llibre, J., Novaes, D. D., & Teixeira, M. A. (2015). On the birth of limit cycles for non-smooth dynamical systems. *Bulletin des Sciences Mathématiques*, *139*(3), 229–244.

Loría, A. (2008). From feedback to cascade-interconnected systems: Breaking the loop. In *Proceedings of the IEEE conference on decision and control* (pp. 4109–4114). Institute of Electrical and Electronics Engineers Inc., http://dx.doi.org/10.1109/CDC.2008.4738647.

Machado, G. F., & Jones, M. (2023). Sparse identification of nonlinear dynamics with side information (SINDy-SI). arXiv preprint arXiv:2310.04227.

Mazare, M., Tolu, S., & Taghizadeh, M. (2022). Adaptive variable impedance control for a modular soft robot manipulator in configuration space. *Meccanica*, *57*(1), 1–15.

Melingui, A., Merzouki, R., Mbede, J. B., Escande, C., & Benoudjit, N. (2014). Neural networks based approach for inverse kinematic modeling of a compact bionic handling assistant trunk. In *2014 IEEE 23rd international symposium on industrial electronics* (pp. 1239–1244). IEEE.

Moreno, J. A., & Osorio, M. (2012). Strict lyapunov functions for the super-twisting algorithm. *IEEE Transactions on Automatic Control*, *57*(4), 1035–1040. http://dx.doi.org/10.1109/TAC.2012.2186179.

Papageorgiou, D., & Edwards, C. (2022). On the behaviour of under-tuned super-twisting sliding mode control loops. *Automatica*, *135*, Article 109983.

Parvaresh, A., & Moosavian, S. A. A. (2021). Dynamics and path tracking of continuum robotic arms using data-driven identification tools. *Robotica*, 1–27.

Quade, M., Abel, M., Nathan Kutz, J., & Brunton, S. L. (2018). Sparse identification of nonlinear dynamics for rapid model recovery. *Chaos. An Interdisciplinary Journal of Nonlinear Science*, *28*(6).

Reinhart, R. F., Shareef, Z., & Steil, J. J. (2017). Hybrid analytical and data-driven modeling for feed-forward robot control. *Sensors*, *17*(2), 311.

Rus, D., & Tolley, M. T. (2015). Design, fabrication and control of soft robots. *Nature*, *521*(7553), 467–475.

Thuruthel, T. G., Ansari, Y., Falotico, E., & Laschi, C. (2018). Control strategies for soft robotic manipulators: A survey. *Soft Robotics*, *5*(2), 149–163.

Thuruthel, T. G., Falotico, E., Renda, F., & Laschi, C. (2017). Learning dynamic models for open loop predictive control of soft robotic manipulators. *Bioinspiration & Biomimetics*, *12*(6), Article 066003.

Thuruthel, T. G., Renda, F., & Iida, F. (2020). First-order dynamic modeling and control of soft robots. *Frontiers in Robotics and AI*, *7*, 95.

Tibshirani, R. (1996). Regression shrinkage and selection via the lasso. *Journal of the Royal Statistical Society. Series B. Statistical Methodology*, *58*(1), 267–288.

Utkin, V. I. (1992). *Sliding modes in control and optimization*. Springer Berlin Heidelberg, Online–Ressource (XVI, 286p. 24 illus) (unknown).

Walker, I. D. (2013). Continuous backbone "continuum" robot manipulators. *International Scholarly Research Notices*, *2013*.

Wang, X., Li, Y., & Kwok, K.-W. (2021). A survey for machine learning-based control of continuum robots. *Frontiers in Robotics and AI*, 280.

Wang, J., Xu, B., Lai, J., Wang, Y., Hu, C., Li, H., et al. (2022). An improved Koopman-MPC framework for data-driven modeling and control of soft actuators. *IEEE Robotics and Automation Letters*, *8*(2), 616–623.